JOURNAL OF GEOPHYSICAL RESEARCH, VOL. 117, B09206, doi:10.1029/2011JB008987, 2012

High-frame rate thermal imagery of Strombolian explosions: Implications for explosive and infrasonic source dynamics

Dario Delle Donne[1] and Maurizio Ripepe[1]

Received 2 November 2011; revised 3 August 2012; accepted 7 August 2012; published 22 September 2012.

[1] Explosive activity at Stromboli volcano is analyzed using a high-frame rate (50 Hz) thermal camera and differential pressure transducers. We develop a thermal image-based decomposition method to derive vertical and horizontal exit velocities of the explosive cloud. Peak vertical velocity ranges between 23 and 203 m/s, slightly higher than previous estimates and rapidly decreasing to a constant value of 30–50 m/s within the first ~0.1 s. Plume velocities are consistent with an elongated cloud expanding much faster vertically than horizontally and indicating the interaction with the conduit wall. Considering a vent radius of ~2 m we estimate a volumetric flux of 200–600 m^3/s, which converts to total volumes of gas-particles of 10^3–10^4 m^3 for a single eruption. These volumes are proportional to the thermal energy recorded by the camera, providing a means to convert thermal radiance to volumes. Comparing the thermal onset of the explosions with the arrival time of the acoustic pressure, we demonstrate that infrasound is propagating 0.14−1.7 s ahead of the explosive front. The time difference between thermal and acoustic onsets constrains the infrasonic source within the conduit at 15–35 m below the crater rim. Peak amplitudes of acoustic pressure show a power law relationship ($p \sim U^2$) with the exit vertical velocities consistent with the energy balance of a two-phase flow rapidly accelerated in the conduit by gas decompression. Our results support monopole isotropic acoustic radiation of a source embedded within the conduit walls and indicate that explosive dynamics undergo strong accelerations of 10^3–10^4 m/s^2.

Citation: Delle Donne, D., and M. Ripepe (2012), High-frame rate thermal imagery of Strombolian explosions: Implications for explosive and infrasonic source dynamics, *J. Geophys. Res.*, *117*, B09206, doi:10.1029/2011JB008987.

1. Introduction

[2] Infrared thermometry has been used to study the explosive dynamics of strombolian activity and to constrain the source process [*Harris et al.*, 2005; *Patrick*, 2005; *Harris and Ripepe*, 2007; *Marchetti et al.*, 2009]. The infrared signal derived from thermal imagery allows one to evaluate several parameters, including the amount of fragments involved in each eruption, the style of activity, the height reached by the ejecta, and the magma output rate (see *Patrick* [2007] and *Ripepe et al.* [2008], among others).

[3] Exit velocity is a vital parameter in evaluating both the dynamics and the energy of an explosive eruption. It is also an important measurement for correct risk assessment as it controls the area affected by fall out [e.g., *Andronico and Pistolesi*, 2010]. Previous attempts to evaluate exit velocities at Stromboli volcano have used different methodologies during different periods of activity, but all give similar values in the range of 10 to 130 m/s [*Chouet et al.*, 1974; *Blackburn et al.*, 1976; *Weill et al.*, 1992; *Ripepe et al.*, 1993; *Seyfried and Hort*, 1999; *Hort et al.*, 2003; *Patrick*, 2007; *Marchetti et al.*, 2009]. This range has thus been considered as the standard velocity range for the typical explosive activity at Stromboli.

[4] Only recently, detailed analyses of high quality thermal imagery and high-speed video camera have revealed the presence of an initial spray of relatively small particles moving at velocities from ~200 m/s [*Harris et al.*, 2012] up to 405 m/s [*Taddeucci et al.*, 2012] within the first 0.5 s.

[5] We have thus analyzed this typical explosive activity of Stromboli volcano using thermal imagery acquired at high frame rates (50 Hz) in order to constrain the exit velocity history and the kinematics of the cloud expansion.

[6] Exit velocities should be theoretically correlated with the excess pressure at the vent [*Woulff and McGetchin*, 1976; *Wilson*, 1980; *Fagents and Wilson*, 1993; *Vergniolle and Brandeis*, 1994; *Johnson*, 2007]. Linear theory of sound demonstrates that infrasound is generated by the volumetric outflow rate of a monopole, dipole or quadrupole source [*Lighthill*, 1978]. Only a few experiments have been carried out to demonstrate that velocities of the volumetric expansion of the gas/fragments cloud and acoustic pressure could be linked [*Johnson*, 2007; *Scharff et al.*, 2008].

[1]Dipartimento Scienze della Terra, Universita' di Firenze, Firenze, Italy.

Corresponding author: M. Ripepe, Dipartimento Scienze della Terra, Universita' di Firenze, v. G. La Pira 4, I-50121 Firenze, Italy. (maurizio.ripepe@unifi.it)

0148-0227/12/2011JB008987

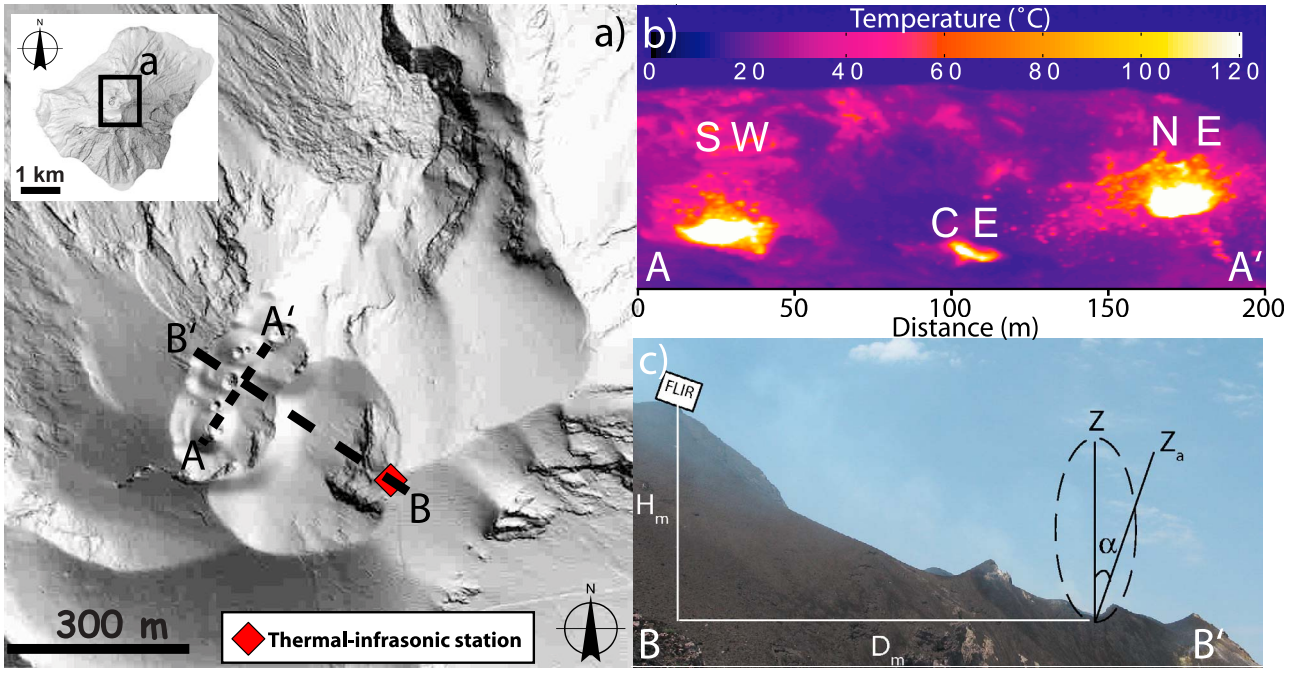

Figure 1. (a) Map of the summit craters of Stromboli volcano (Italy) and location of the FLIR A-20 thermal camera and the infrasonic sensor. (b) Position of the three craters along the terrace (A-A′ section in Figure 1a) and (c) position of the thermal camera with the horizontal (D_m) and vertical (H_m) distances from the NE craters (B-B′ section in Figure 1a) calculated using high-resolution topographic data; Z and Z_a are the real and apparent heights of the eruptions that are related to the inclination angle α.

[7] In this work we present a method to measure the exit velocity in real-time using high-frame rate thermal imagery. We demonstrate that infrasound, during our experiment, is generated within the conduit >0.14 s before the hot gas cloud begins to expand in the atmosphere. We show that only a small portion of the infrasonic signal might be generated outside the conduit during the expansion in the atmosphere of the gas/fragments cloud. We show that infrasound is linked to source dynamics acting inside the conduit and not by gas expansion outside the vent. However, thermally derived maximum exit velocities at the vent and measured peak infrasonic pressures generated inside the conduit are well correlated, suggesting a strong link to the explosive mechanism.

2. Instrument Setup

[8] Explosive activity was recorded with a thermal camera and acoustic sensors during four consecutive days at the summit of the Stromboli volcano from 5th to 9th May 2008 (Figure 1). During data acquisition, explosive activity was relatively high, being characterized by ballistics ascending to ~200 m above vents in NE and SW craters.

[9] We used a *FLIR-A20* thermal camera with a 34° × 25° optical lens (9.2 mm), and 0.1°C thermal resolution. The sensor is an un-cooled micro-bolometer focal plane array of 160 × 120 pixels, which is electronically oversampled at 320 × 240 pixels, and sensitive in the 7.5–13 μm spectral range. Thermal images were collected at a frame rate of 50 Hz using Thermacam Researcher® acquisition software by Firewire connection.

[10] Infrasound was recorded using an iTem prs-0100x differential pressure transducer with a sensitivity of 25 mV/Pa at 1 Hz and with a flat frequency response of 0.01–100 Hz at a full scale range of 250 Pa. Infrasound was digitized using a 24 bit Guralp CMG24 Digitizer at 100 Hz. Thermal images and infrasound were synchronized using the same GPS clock with an accuracy of ~5 ms.

[11] The infrasonic sensors and the thermal camera were located at Pizzo Sopra La Fossa from where both the NE and SW craters could be viewed (Figures 1a and 1b). The distance (D) between the acquisition system and the active vents was estimated from laser range finder measurements. These gave a distance of 345 m to the NE crater and 327 m to the SW crater (Figure 1). Using a high-resolution DEM (Digital Elevation Model) with a cell size of 5 × 5 m we calculated the difference in elevation between the craters and the acquisition site (H_m) to be of 184 m. The horizontal distance to the two studied craters (D_m) was calculated to be 292 m to the NE crater and 270 m to the SW crater.

3. Focal Plane Correction

[12] We assume that gas, ash and bombs form an explosive cloud which is accelerated within the conduit by the same source dynamics and at the same time. Each component of the cloud will have different velocities related to their mass, with the gas moving faster than the bombs and thus leaving the conduit at a different time [e.g., *Chouet et al.*, 1974; *Steinberg and Babenko*, 1978; *Ripepe et al.*, 1993; *Pistolesi et al.*, 2011]. Pure gas has a very low thermal emissivity (ε < 0.2) and it is not visible on the thermal

camera. However, volcanic ash has a higher thermal emissivity ($\varepsilon \sim 0.96$) [*Harris and Stevenson*, 1997] and travels at a velocity close to that of the gas. We thus consider that the ash acts as a tracer for the invisible gas component. The maximum exit velocities derived by thermal image analysis can then be considered as representative of the velocity of the gas jet.

[13] To calculate reliable exit velocities, thermal images first need to be corrected for the inclination of the focal plane, and the pixel size has to be calculated according to the slant distance and the angular aperture of the camera lens.

[14] Assuming a vertical jet emission Z, the apparent vertical trajectory in the images (Z_a) is given by $Z_a = Z^*\cos(\alpha)$, where α is the angle between the camera plane and the vertical trajectory of the particle (Figure 1c). The inclination (α) of the focal plane is calculated from $\alpha = \tan^{-1}(H_m/D_m)$ using the horizontal distance D_m and the difference in elevation H_m between the recording site and the target. The camera was accordingly inclined of 32° and 34° when looking at the NE and SW crater, respectively.

[15] Pixel size of thermal images of NE crater eruptions were thus calculated using the image vertical field-of-view of 25°, which in the planar view approximation, and at a distance D = 345 m, is equivalent to 153 m. For a 320 × 240 pixel image, the size of each pixel h_{pxl} is thus 0.64 m, which represents the vertical resolution used to track the objects ejected by the NE crater. Number of pixels (N_{pxl}) along a line is thus converted to vertical heights $h = N_{pxl}{}^*h_{pxl}/\cos(\alpha)$ using the inclination (α) of the focal plane. This method is valid only in the assumption of a nearly vertical trajectory of the volcanic jet and of no spherical aberration of the FOV. Using the same methodology described for the vertical axis and assuming a horizontal symmetry of the thermal camera focal plane, we convert number of pixels in the horizontal component into meters using the horizontal field-of-view of 34°.

4. Thermal Decomposition Image Processing

[16] To estimate the exit velocity of the gas-ash mixture, thermal images were processed using multiple temperature thresholds (τ) from 50° to 250°C with steps of 50°C. The temperature contour lines derived in consecutive frames (Figure 2) allowed us to track the vertical and horizontal position of the plume front and the thermal structure within the plume.

[17] Temperature is generally higher inside the plume core and it gradually decays with distance from the core. The temperature gradient between the plume and the ambient background is also characterized by a sharp contrast. This makes the plume leading edge easy to track using the most external thermal contour line (Figure 2a). The use of multiple temperature thresholds thus allows us to track hot bodies moving inside the leading edge of the plume and to obtain a more stable solution for the plume exit velocity. The total number of pixels above each thermal threshold gives the area covered by the gas-particle mixture, and allows a rough estimate of the cloud volume above each temperature threshold.

[18] Using different temperature thresholds (τ), we convert each pixel in the original temperature frame $T(t,x,y)$ into binary frames $T_b(t,x,y,\tau)$ by assuming values of $T_b = 0$ when pixels temperature are below τ and values of $T_b = 1$ when pixels temperature are above τ:

$$T_b(t,x,y,\tau) = \begin{matrix} 1 \\ 0 \end{matrix} \left| \begin{matrix} T(t,x,y) \geq \tau \\ T(t,x,y) < \tau \end{matrix} \right. \quad (1)$$

where x and y are the coordinates of the pixel inside each frame.

[19] The binary image T_b can thus be converted into two temperatures distribution functions representing the vertical (T_z) and the horizontal (T_h) sum of all the binary values along the x row and the y column of the image:

$$\begin{aligned} T_z(t,x,\tau) &= \sum_{y=1}^{Ny} T_b(t,x,y,\tau) \\ T_h(t,y,\tau) &= \sum_{x=1}^{Nx} T_b(t,x,y,\tau) \end{aligned} \quad (2)$$

where Nx (=320) and Ny (=240) are the vertical and the horizontal number of pixels in the image, respectively.

[20] The two new functions $T_z(t,x,\tau)$ and $T_h(t,y,\tau)$ thus represent the distribution of the number of pixels with a temperature above a given threshold at a given time (Figure 3) in the horizontal x and vertical y frame direction. Finally, we assume that the maximum values $Z(t,\tau)$ and $H(t,\tau)$ of the two functions $T_z(t,x,\tau)$ and $T_h(t,y,\tau)$ represent the edge of the plume in the vertical (x) and horizontal (y) direction, respectively.

[21] The first time derivatives of $Z(t,\tau)$ and $H(t,\tau)$ for each temperature threshold:

$$\begin{aligned} u(t,\tau) &= \frac{\partial Z(t,\tau)}{\partial t} \\ w(t,\tau) &= \frac{\partial H(t,\tau)}{\partial t} \end{aligned} \quad (3)$$

are used to calculate vertical $u(t,\tau)$ and horizontal $w(t,\tau)$ plume exit velocities.

[22] This method is based on decomposition of the thermal images and allows us to track, in real-time, plume expansion in the atmosphere and to automatically derive height and exit velocity.

[23] To check the reliability of this automatic image processing procedure, the vertical and horizontal velocities were also calculated by manually picking the more external contour of the $T_z(t,x,\tau)$ and $T_h(t,y,\tau)$ distributions. The real-time thermal decomposition and the manual picking methods both gave similar results.

[24] Plume height increases with time coherently for each temperature threshold, but the higher temperature thresholds (Figure 2b) better constrain the onset velocity encountered at the beginning of each emission. We thus considered the plume velocity history as the set of the maximum values $U(t) \geq \{u(t,\tau)\}$ and $W(t) \geq \{w(t,\tau)\}$ between all the vertical and horizontal velocities for each temperature threshold, respectively (Figure 2c).

5. Vertical and Horizontal Plume Velocities

[25] Comparison of vertical and horizontal velocity profiles shows that 1) vertical velocities are usually greater than the horizontal velocities and 2) maximum vertical and

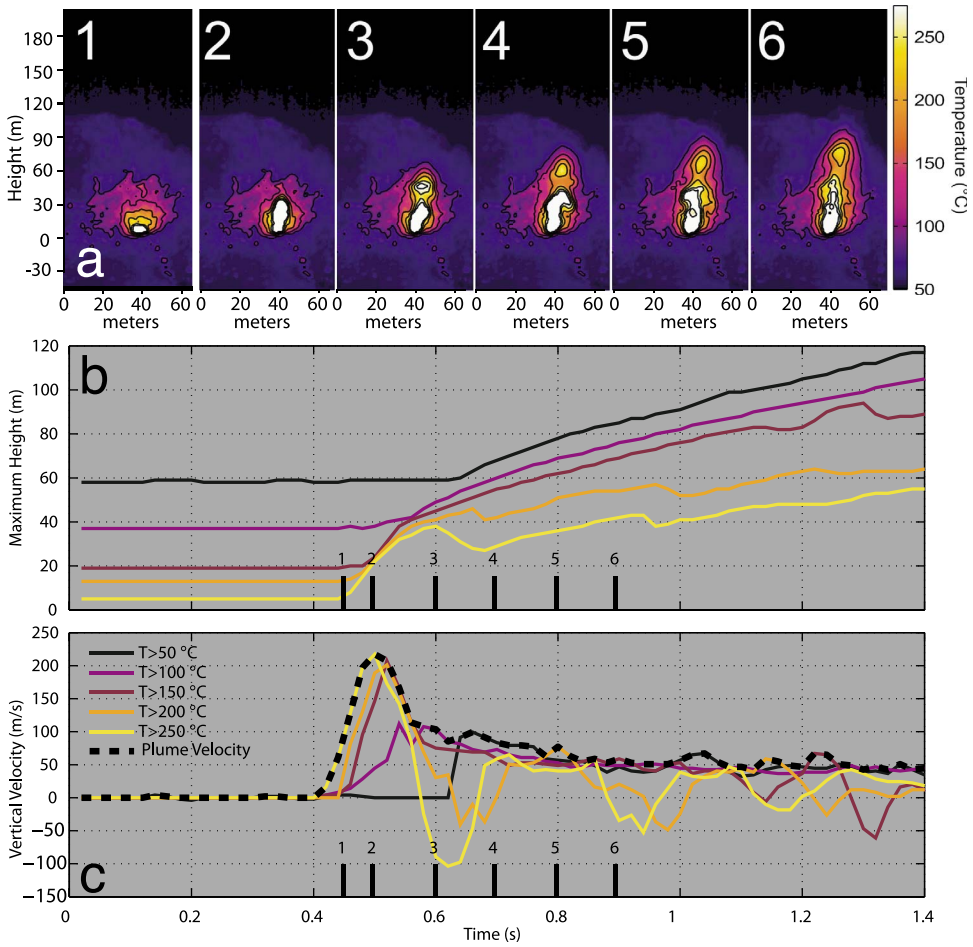

Figure 2. (a) Example of plume tracking using the thermal decomposition method with different thresholds at 50, 100, 150, 200 and 250°C (5th May 2008, 16:38 GMT, NE crater). (b) Plume height tracked using different temperature thresholds; higher temperature thresholds are more sensitive to the eruption onset whereas lower temperature thresholds better define the plume evolution in its late stage. (c) Vertical velocity of the plume calculated using different temperature thresholds. The final plume velocity (black dashed line) is estimated in each frame using the maximum vertical velocity measured among the different temperature thresholds. The marks in Figures 2b and 2c are related to the numbering of each frame in Figure 2a.

horizontal velocities are not positively correlated (Figure 4). This is consistent with a finger jet-like explosion having an expansion axis mainly oriented in the vertical direction. Plume expansion is thus strongly controlled by the conduit geometry and occurs mainly vertically with a minor but still consistent horizontal component.

[26] Peak vertical and horizontal velocities (Figure 4) range between 23 and 203 m/s with a resolution of ±16 m/s, considering a pixel size of 0.64 m and a sampling rate of 0.02 s. These velocities are somewhat higher than previous measurements using lower sampling rates [*Chouet et al.*, 1974; *Weill et al.*, 1992; *Ripepe et al.*, 1993; *Seyfried and Hort*, 1999; *Patrick*, 2007; *Ripepe et al.*, 2008] but are representative for the first ~0.1 s and this explains why such higher velocities have not been reported before. However, these are in very good agreement with the velocities of 213 m/s calculated during recent experiments using high-quality thermal imagery [*Harris et al.*, 2012] and represents the lower limit of the particle velocities range (from 172 to 405 m/s) detected by high-speed video camera [*Taddeucci et al.*, 2012].

[27] After the first 0.1 s the plume decelerates and the explosion dynamics evolve at a constant velocity regime of 20–50 m/s with a nearly constant plume expansion rate.

6. The Gas Thrust Phase

[28] Strombolian plumes are generally described by two main dynamic phases. During the first phase, ascent of the volcanic plume is driven by the gas thrust, after which the plume rises at a constant velocity due to buoyancy, slowly expanding in the atmosphere with the entrainment of air [*Wilson*, 1980; *Patrick*, 2007].

[29] The gas thrust phase feeds new hot ash and fragments into the thermal camera FOV and it is hence responsible for the increase in temperature, with the plume velocity decreasing as plume height increases. The buoyancy phase is instead associated with the waning plume temperatures,

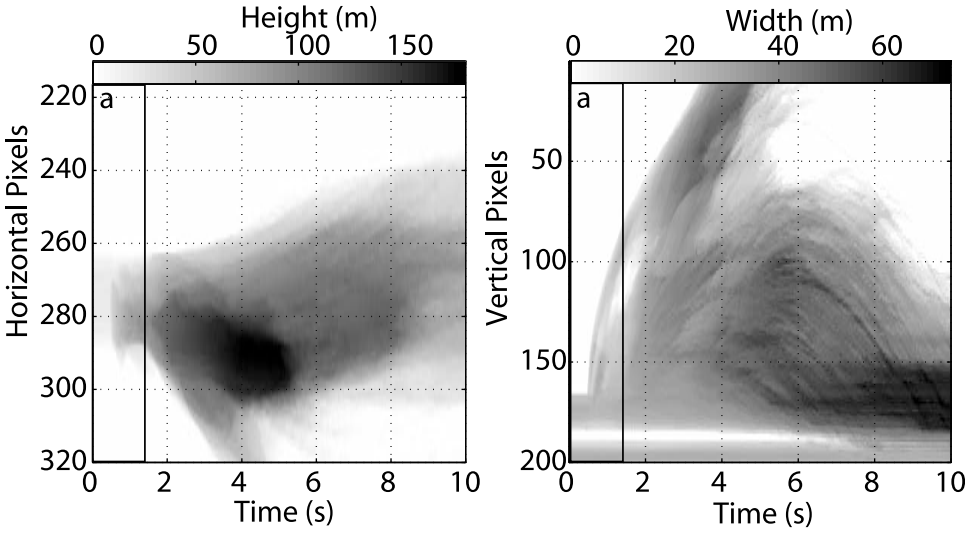

Figure 3. Example of temperature distribution functions along the horizontal (T_z) and vertical (T_h) axis for 150°C temperature threshold. Vertical and horizontal pixels are the same as Figure 2a, whereas the insets are indicating the time interval represented in Figures 2b and 2c.

since no volcanic material is ejected anymore. The plume is rather expanding by air entrainment during its convective rise thereby reducing its internal temperature [*Wilson*, 1980; *Patrick*, 2007; *Marchetti et al.*, 2009].

[30] The time history of the plume exit velocity nicely shows these two main phases of explosive dynamics (Figure 5) with a well-defined gas thrust phase lasting for 3–4 s and followed by a buoyancy phase of 6–7 s.

[31] The high frame rate of the thermal images reveals that the gas thrust is characterized by two different stages. In the first ∼150 ms, the gas thrust shows exit velocities up to ∼200 m/s, then it rapidly decelerates in ∼200 ms to a regime of almost constant velocity at ∼40 m/s and lasting for ∼3–4 s. During deceleration and the constant velocity regime, gas thrust is still feeding the plume pushing the hot gas and fragments up to the maximum heights of 100–200 m.

[32] The evidence of two stages during the gas thrust phase indicates explosive dynamics characterized by a sharp high value in the mass discharge followed by a lower but constant regime of mass flux.

[33] After the gas thrust phase, velocities decrease down to <10 m/s, typical of a buoyant rise regime. The plume slowly rises up entraining air and showing a gradual decrease in the temperatures for another ∼6–7 s. Then, plume height and ascent velocity decrease coherent as the plume dissipates. Consistent with previous analysis [e.g *Patrick*, 2007], total duration of a typical Strombolian explosion is of ∼10–12 s.

7. Plume Volumes and Thermal Energy

[34] Considering a vent radius a of ∼2 m (±0.35 m), as estimated from the thermal images and field observations during the experiment (Figure 1b), we can use the vertical velocity profile $U(t)$ to evaluate the plume volume flux $\Phi(t) = \pi a^2 U(t)$. Results range between 200 and 600 m^3/s. By integrating the volume flux through time, we calculate that the plumes have a total volume (V_{plume}) ranging between 300 and 3000 m^3 (Figure 6). These values are in agreement with previous gas volume estimates using COSPEC and thermal images analyses [*Allard et al.*, 1994; *Harris and Ripepe*, 2007] and with recent gas volume measurements of $\sim 10^3$ m^3 using OP-FTIR [*Mori and Burton*, 2009].

[35] Integrating the mean temperature within the image FOV of the thermal camera and by using the Stefan-Boltzmann law [e.g., *Marchetti et al.*, 2009], we can also calculate the apparent thermal energy radiated during each explosion:

$$E_T = \varepsilon \sigma A_{FOV} \int_t T^4 - T_{BKG}^4 dt \quad (4)$$

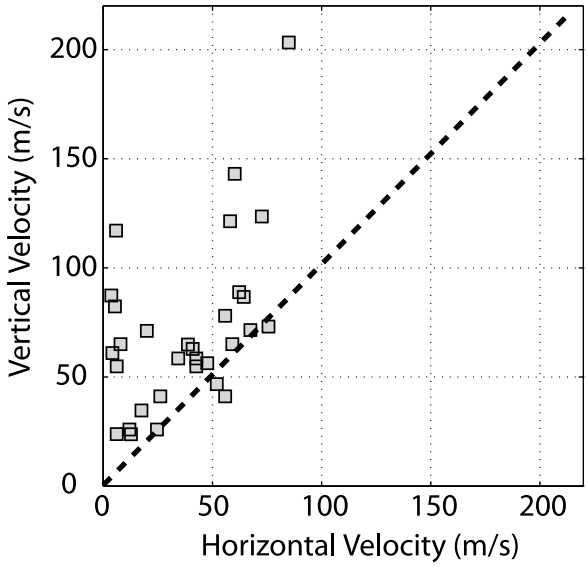

Figure 4. Peak vertical and horizontal exit velocities for the 31 analyzed eruptions. Black dashed line indicates the 1:1 ratio typical of a spherical expansion. Most of the eruptions remain in the upper portion of the plot indicating that horizontal velocities are often smaller than vertical velocities and thus indicating a jet-like plume kinematics.

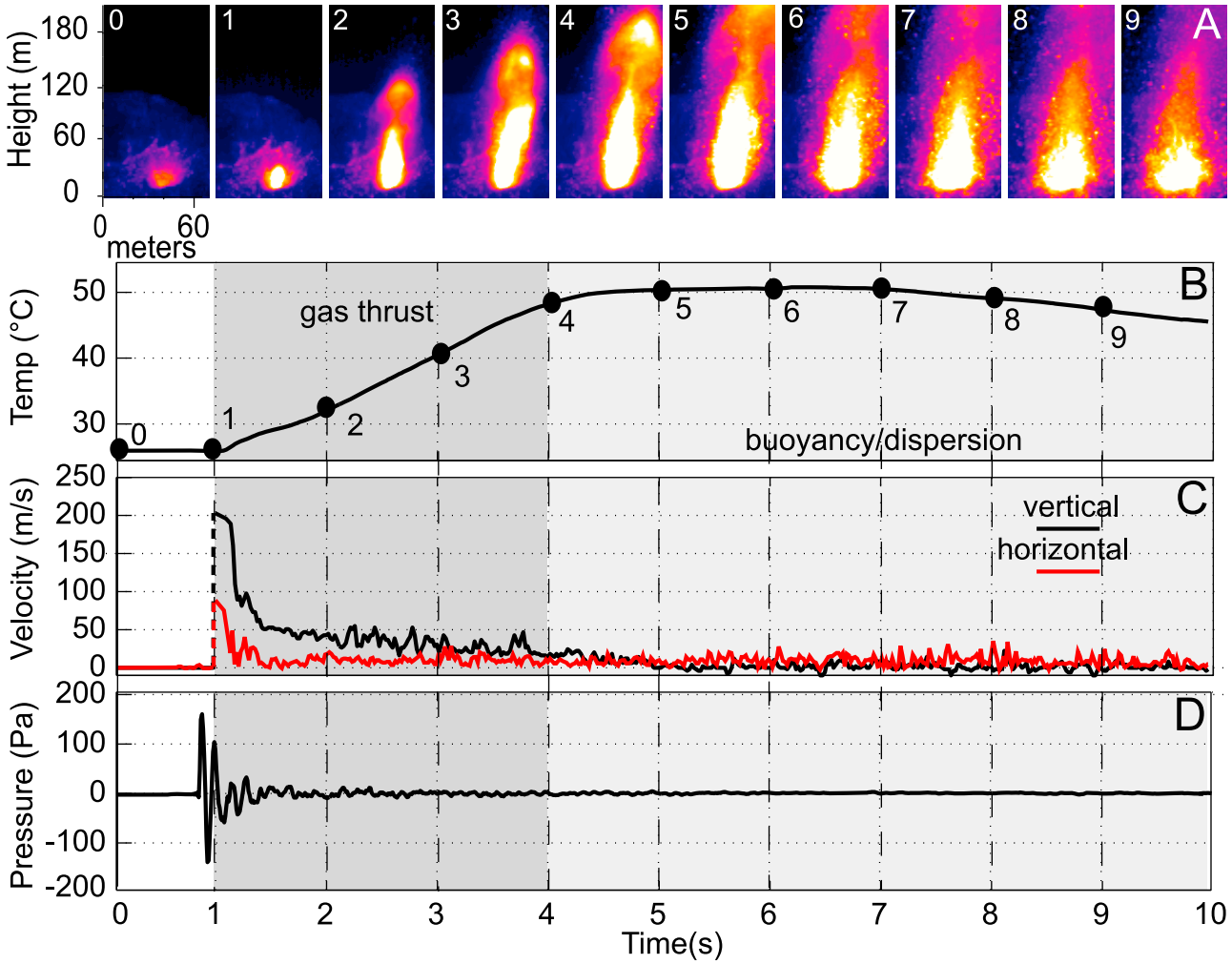

Figure 5. Thermal and acoustic signature of a strombolian eruption (5th May 2008, 16:38 GMT, NE crater). (a) Snapshots of the eruption from the NE crater taken at 1 s intervals. Frames have been numbered and reported on each of the functions below. (b) Temperature of the explosion integrated in the FOV. The end of the gas thrust phase coincides with the maximum height reached by the plume and by the maximum peak temperature (frame 4), After frame #4 large part of the heavier fragments start to fall-down while the gas and fine ash keep to rise buoyantly (from frame 5–9). (c) Vertical and horizontal velocities derived by the thermal decomposition analysis reveal high initial exit velocities followed by a rapid deceleration to a steady (uniform velocity) dynamics (from frame 1–4). After frame 4 the buoyancy phase is characterized by lower velocities. (d) Infrasound associated with this explosion has been corrected for the theoretical reduced time at the vent (Δ_{tr}) and shows that the acoustic waves are generated before the gas/ash mixture comes out of the vent. The highest acoustic amplitude is thus generated within the conduit and is not related to the plume dynamics outside the vent. During the buoyancy/dispersion phase no significant infrasound is generated.

where E_T is the apparent radiated thermal energy (in Joules), ε is the ash emissivity (~0.96) [*Harris and Stevenson*, 1997], σ is the Stefan-Boltzmann constant, A_{FOV} is the area of the field of view, T is the integrated temperature within the FOV, and T_{BKG} is the background temperature in the FOV evaluated just before the eruption onset.

[36] Because volcanic gas is characterized by a very weak emissivity, the main contribution to the radiated thermal energy will be due to the erupted volcanic ash and bombs. The thermal energy spans two orders of magnitude between 10^6 and 10^8 Joules [*Marchetti et al.*, 2009].

[37] Total plume volume calculated from the thermally derived exit velocities correlates well (0.93) with the thermal energy (Figure 6):

$$\log(V_{plume}) = 0.35\log(E_T) + 0.74 \quad (5)$$

where the slope (0.35) and the intercept (0.74) depend on the distance of the camera from the crater and the density of the cloud.

[38] However, this relationship cannot be considered a general law to calculate plume volumes from thermal imagery, but does represent evidence that thermal radiance is

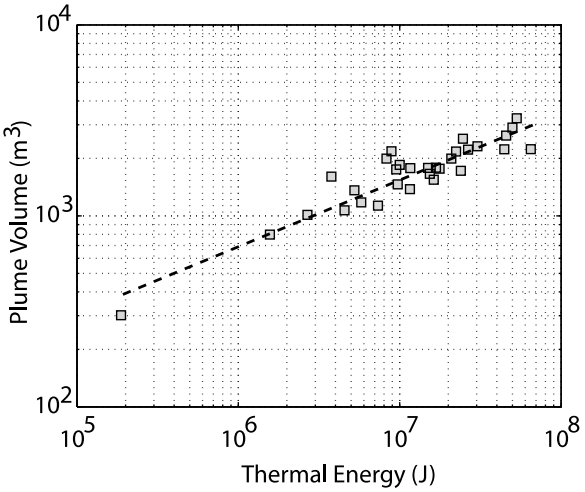

Figure 6. Total erupted plume volume estimated from the thermally derived vertical velocities show a good correlation with the total radiated thermal energy for all 31 eruptions. This indicates that thermal energy can be considered as a good proxy to the volume (and therefore mass) of the ejected material.

linked to volumes of juvenile ash and fragments ejected. This is also coherent with previous experiments, which have shown that the amplitude of the thermal energy is also well correlated both with the total mass of the explosions estimated from thermal camera imagery [*Patrick*, 2005] as well as with the total reflected energy detected by the Doppler radar [*Scharff et al.*, 2008].

[39] Equation (5) also has for Stromboli volcano strong monitoring implications, representing a method that allows quick measurements of the volume of the gas/ash fragments erupted directly from the integration of the thermal radiance waveforms.

8. Position of the Infrasonic Source

[40] To understand which phase of the plume dynamics is generating infrasound, we calculated the time delay between the infrasound and the thermal onset for each explosion (Figure 7). The crater terrace at Stromboli collapsed during the 2007 eruption [*Barberi et al.*, 2009] and thus offers an unprecedented opportunity to look directly into the vents with no topographic obstruction along the line-of-sight.

[41] The theoretical travel time (t_r) of infrasound is estimated considering the slant distance (D) between the recording site and the SW crater (327 m), or the NE crater (345 m), and assuming a constant sound velocity of c = 340 m/s (900 m elevation, 15°C atmospheric temperature). We calculated two arrival times $t_r = D/c$ of 0.96 and 1.01 s for the sound to travel from the SW and NE vents to the sensor, respectively.

[42] If infrasound is generated at the vent by the expansion of the gas in the atmosphere then the time delay $\Delta t = t_{\exp} - t_{acu}$ between the acoustic (t_{acu}) and thermal ($t_{\exp}$) should be equal to the travel time t_r. For such condition the reduced time delay $\Delta t_r = t_{\exp} - t_{acu} + t_r$ should be 0.

[43] The analyzed explosions have reduced time delays of between 0.14 s and 1.7 s, which are incompatible with an at-surface position for the source. This evidence is in line with previous measurements [*Ripepe et al.*, 2001] and demonstrates that infrasound is generated by a dynamic process

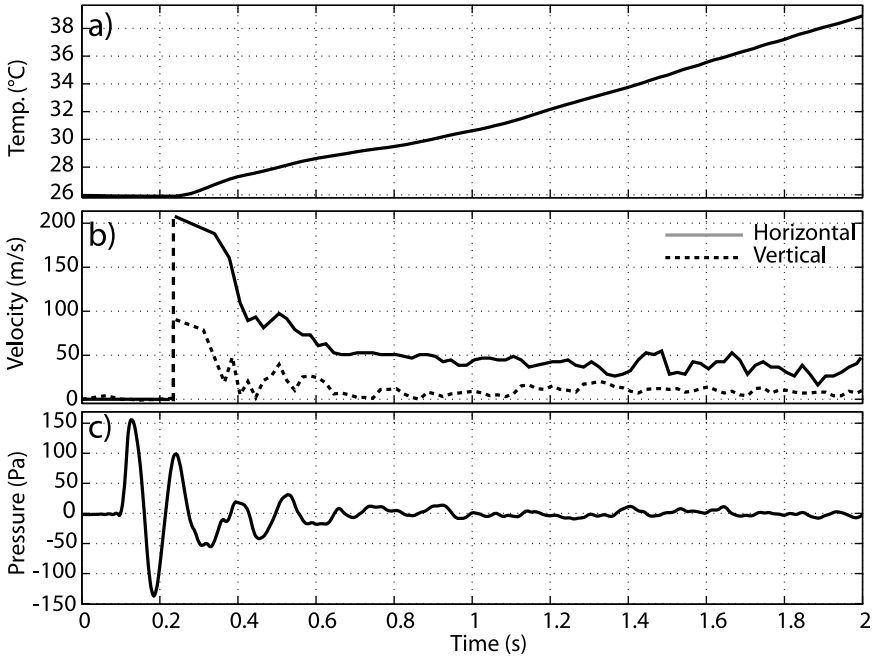

Figure 7. Close-up of the first 2 s of the explosion shown in Figure 5 highlighting the early gas-thrust phase lasting for ~0.1 s characterized by (a) sharp step in the temperature trace and (b) the highest plume velocity. During the plume expansion phase in the atmosphere only a small part of (c) infrasound is produced.

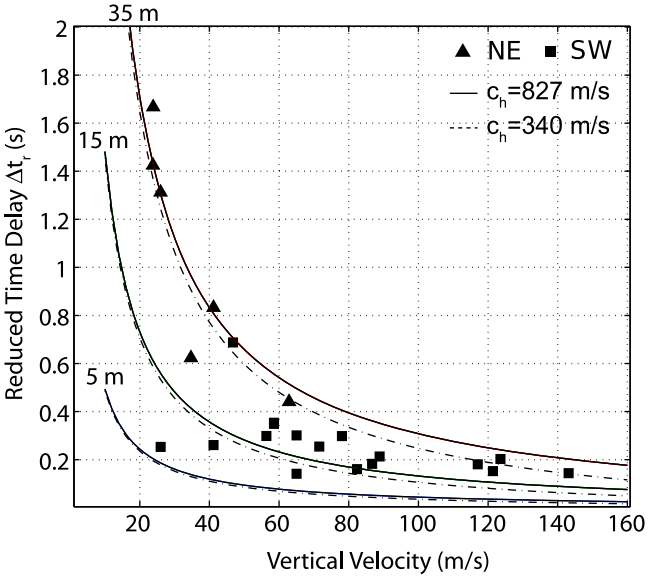

Figure 8. The reduced time delays plotted against the peak vertical velocities are in good agreement with the explosive model represented by equation (6). It indicates a position of the acoustic source <15 m at the SW crater, and <35 m at the NE crater during the acquisition period.

acting inside the conduit before the gas and ash plume expand in the atmosphere.

[44] Once the infrasonic record is reduced to the vent using the theoretical travel time t_r, we observe (Figure 7) that only a small component of the infrasonic wavefield might be generated during the gas-ash cloud expansion in the atmosphere.

[45] In fact, only the first short-lived (<150 ms) gas-thrust phase, characterized by high exit velocities is correlated in time with small amplitude infrasonic waves. The second long-lasting (~4 s) stage of the gas thrust phase with constant exit velocity (~50 m/s) does not produce infrasonic waves. The largest initial infrasonic peak is generated before the emission onset, and thus most of the acoustic energy is radiated before the plume reaches the surface (Figure 7).

[46] The reduced time delay Δt_r also correlates with the inverse ($\Delta t_r \sim U^{-1}$) of the exit velocity (Figure 8). This can be explained only if the infrasound has its origin within the conduit.

[47] We have no direct measurements of the gas velocity in the conduit but we assume that the gas-ash cloud is violently accelerated at the onset of the explosions to quickly reach its maximum velocity within the conduit. In this case, the reduced time delay (Δt_r) and the exit velocity U can be used to estimate the position of the infrasonic source inside the conduit [*Ripepe et al.*, 2001]:

$$h_c = \Delta t_r \left(\frac{c_h U}{c_h - U} \right) \tag{6}$$

where h_c is the depth of the source and c_h is the speed of sound inside the conduit. Assuming here that sound speed c_h in the conduit is constant and it can range between 340 m/s (for an atmosphere in the conduit at ambient temperature) to 827 m/s (for an atmosphere in the conduit at 1050 K in equilibrium with the magma), we estimate that infrasound has its origin at a depth <35 m inside the NE crater and <15 m inside the SW (Figure 8).

9. Acoustic Pressure and Plume Exit Velocities

[48] Our measurements provide evidence for an infrasonic source embedded in the conduit. This conclusion is not new. Infrasonic waves have already been explained as being generated within the conduit at the magma free surface [e.g., *Garcés*, 2000; *Ripepe et al.*, 2001; *Kobayashi et al.*, 2005; *Ruiz et al.*, 2006; *Petersen and McNutt*, 2007; *Johnson*, 2007]. The correlation of high-frame rate thermal imagery and acoustic recordings supports and corroborates this general view and provides new evidence that infrasound is not produced by the expansion of the gas in the atmosphere.

[49] According to the linear theory of sound [*Lighthill*, 1978], acoustic pressure propagating in a homogeneous atmosphere and recorded at a distance r from the source can be expressed in terms of a rate of change in the volumetric outflow $\dot{V}(t)$:

$$p(t) = \frac{\rho_o}{2\pi \mathrm{r}} \ddot{V}(t - r/c) \tag{7}$$

where ρ_o is the density of the air (=1.08 kg/m^3 at ~900 m of elevation and for an ambient temperature of 15°C).

[50] When the magma surface is deforming and expanding, it will produce an equivalent displacement of the atmosphere, inducing a volumetric compression and generating an excess of pressure that is related to the rate of volumetric change of the atmosphere displaced. In the far-field condition (for acoustic wavelength that is much larger than source dimension), the velocity U_o of the expanding volume can be related to the acoustic power Π [*Woulff and McGetchin*, 1976]:

$$\Pi = K_m \frac{2\pi \mathrm{R}^2 \rho_o U_o^4}{c} \tag{8a}$$

$$\Pi = K_d \frac{\pi R^2 \rho_o U_o^6}{c^3} \tag{8b}$$

$$\Pi = K_q \frac{\pi R^2 \rho_o U_o^8}{c^5} \tag{8c}$$

This applies to a monopole (8a), dipole (8b) or quadrupole (8c) source [see *Caplan-Auerbach et al.*, 2010 and references therein] where R is the source dimension and the coefficients K_m, K_d and K_q are empirical constants equal to 1, 10^{-2} and 10^{-5}, respectively [*Vergniolle and Caplan-Auerbach*, 2006].

[51] A monopole source is typically related to isotropic radiation of the volumetric acceleration in the atmosphere. In general, artificial blasts and strombolian explosions have been explained in terms of acoustic monopoles [e.g., *Vergniolle and Brandeis*, 1994]. Dipole sources have been used to explain vulcanian eruptions involving large amounts of solid particles [*Vergniolle and Caplan-Auerbach*, 2006; *Caplan-Auerbach et al.*, 2010] and can be explained by the

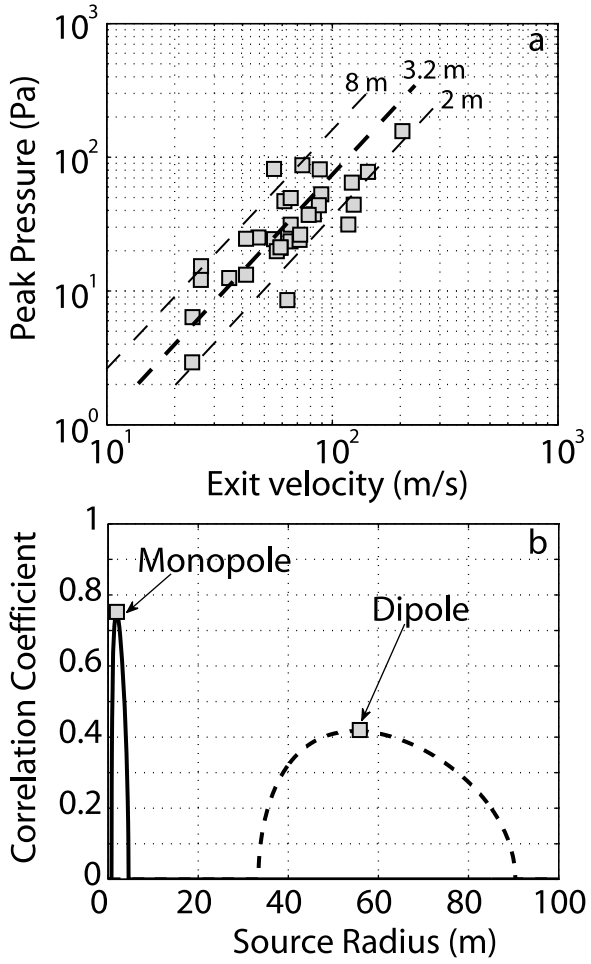

Figure 9. (a) Peak vertical velocities and maximum excess pressures for 31 explosions. Logarithmic fit shows a correlation coefficient of 0.8. The slope of the linear fit (1.9) is consistent with an acoustic source represented by a monopole, while the intercept value of −1.95 allows to estimate a source radius of 3.2 m. The dashed lines represent the linear solution for a radius of 2 and 8 m, respectively. (b) Correlation coefficient as a function of the vent radius for a monopole and dipole source. The maximum correlation coefficient ∼0.75 is given for a monopole model with 1.88 m vent radius. The correlation coefficient becomes worse (∼0.42) when a dipole source model is considered. Besides the distribution of possible solutions is ranging between 35 and 90 m of radius. This is much larger than what is observed at Stromboli.

interaction of the gas jet with the solid boundary of the conduit, which provides an external force on the flow. Quadrupole source is associated with a momentum changes during large jet-like sub-plinian eruption [*Matoza et al.*, 2010] and involves turbulent flow dynamics.

[52] Because the acoustic power in a hemispheric area is directly related to the excess pressure in the atmosphere recorded as acoustic waves [*Lighthill*, 1978]:

$$\Pi = \frac{2\pi r^2}{\rho_o c} p^2 \tag{9}$$

it is possible, using equations (8) and (9), to relate the acoustic pressure (p) to the velocity (U_o) of the volumetric flux changes for a monopole, dipole or quadrupole source:

$$\langle p \rangle = \frac{\rho_o R \sqrt{K_m}}{r} U_o^2 \tag{10a}$$

$$\langle p \rangle = \frac{\rho_o R \sqrt{K_d}}{rc} U_o^3 \tag{10b}$$

$$\langle p \rangle = \frac{\rho_o R \sqrt{K_q}}{rc^2} U_o^4 \tag{10c}$$

where $\langle p \rangle = \sqrt{p^2}$ is the first positive peak of the recorded acoustic pressure. In their logarithmic form $\log(p) = m\log(U_o) + n$, these equations becomes a linear function in which the slope (m) varies between 2 for a monopole, 3 for a dipole, and 4 for a quadrupole source.

[53] The ratio between the acoustic pressure and the velocity of the volumetric change in the logarithmic scale will thus indicate which among the three possible acoustic sources is better representing the explosive dynamics within the conduit.

[54] However, we do not have direct measurements of the velocity U_o inside the conduit and hence we assume here as first approximation that the explosive mix of gas and particles is quickly accelerated to its maximum exit velocity U inside the conduit, such as $U_o = U$.

[55] The first positive acoustic pressure peak (p) measured at Stromboli shows a linear correlation ∼0.8 with initial exit velocity (U) measured by thermal decomposition analysis (Figure 9a). The calculated linear fit has a slope m of 1.9, which is very close to that expected for a monopole, which suggests that at Stromboli acoustic pressure is most likely generated by a monopole. This result is consistent with previous conclusions on the acoustic source generated by explosions at Stromboli [*Vergniolle and Brandeis*, 1994] and with the physical nature of artificial blast. Assuming that air density and source radius remain constant in time, from the intercept $n = \log\left(\rho_o R\sqrt{K_m}/r\right) = -1.95$ we calculate a source radius R of 3.2 m, which is very close to the vent radius a∼2 m we estimated by thermal images.

[56] Considering possible inaccuracy in the pressure amplitude (±0.01 Pa) and exit velocities (±16 m/s) measurements due to instrument self-noise and resolution bias, we forced the ratio m to be exactly 2 (equation (10a)). In this case, the best fit with the measured data set slightly decreases to 0.75 and the new intercept $n = -2.18$ is consistent with a source radius R of 1.88 m (Figure 9b). This is still in very good agreement with our direct observation of the vent dimension (∼2 m).

[57] However, directivity of the gas thrust phase seems more consistent with a dipole source where gas expansion is strongly controlled by the conduit walls [*Caplan-Auerbach et al.*, 2010; *Johnson et al.*, 2008]. To test this possibility, we forced the ratio between the measured excess pressures and the thermally derived exit velocities to be equal to 3 ($p \sim U^3$ - equation (10b)).

[58] The best linear fit with the logarithmic form of equation (10b) decreases to 0.42, with the intercept

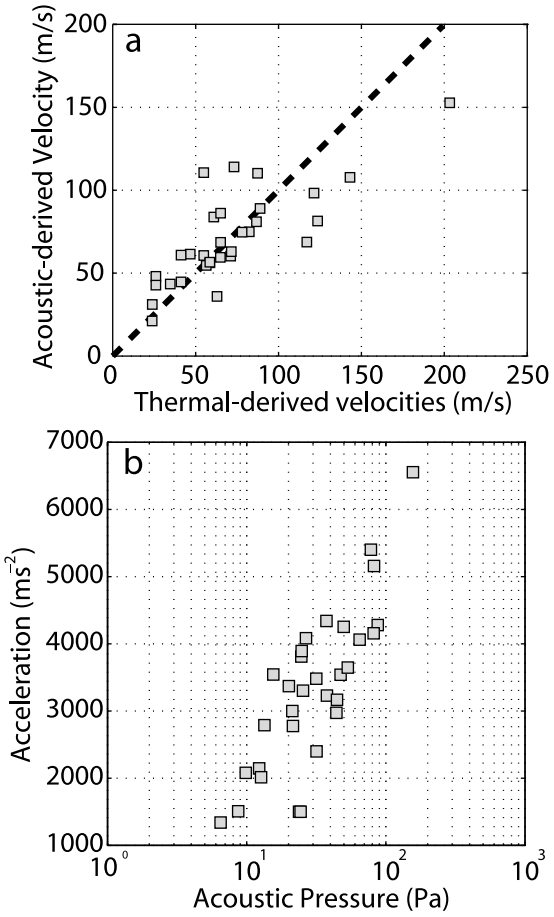

Figure 10. (a) Thermally derived maximum vertical velocities U show a good correlation (0.78) with the velocity U_o calculated (equation (10a)) from the first peak of the acoustic signal assuming a monopole. (b) Accelerations of the initial gas thrust phase inside the conduit are calculated by the first derivative of the infrasonic velocity history are ranging between 1250 and 6700 m/s^2.

$n = \log\left(\rho_{air} R\sqrt{K_d}/rc\right)$ of −3.84 being consistent with a source radius of 55 m (Figure 9b). This is one order of magnitude greater than the vent width observed at Stromboli.

[59] Our measurements thus suggest that the infrasonic source at Stromboli is compatible more with a monopole rather than with a dipole. We then use equation (10a) to calculate the velocity (U_o) of the volumetric change of the source from the recorded acoustic pressure (p). The good correlation (0.78) with the exit velocities (U) derived by thermal decomposition analysis (Figure 10a) indicates that the gas-fragments mixture is accelerated in the conduit to its maximum flow velocity within hundreds of milliseconds.

[60] The velocity history derived from the acoustic records shows that the volumetric change of the source lasts 0.1–0.3 s, which is much shorter than the total duration of the gas thrust phase (4–5 s) observed in the thermal images (Figures 5). This indicates that the duration of the explosive fragmentation is one order of magnitude shorter than the duration of the gas thrust phase.

[61] By time differentiation of the acoustically derived velocity history (equation (10a)), we calculate that source volume expansion in the conduit accelerates at between 1250 and 6700 m/s^2 (Figure 10b), thus compressing the air above the magma surface and generating the acoustic wavefield. After that, the explosive flow becomes stationary and no further significant infrasound is produced during the gas thrust phase.

10. Conclusion

[62] Thermal imagery acquired at high-frame rates (50 Hz) shows that strombolian explosion can be characterized by plume exit velocity higher than those previously reported using lower (0.25–4 Hz) sampling rates. The thermal decomposition method based on different temperature thresholds reveals that the gas thrust phase is characterized by an extremely high initial exit velocity of up to 203 ± 16 m/s for ∼0.1 s, followed by a sharp deceleration down to a slower, but constant gas thrust regime of ∼50 m/s lasting for 4–5 s. Following this, buoyancy takes over and controls the plume dynamics.

[63] Exit velocities of the gas/fragments cloud derived using the thermal decomposition method can be used to estimate volume fluxes of 200–600 m^3/s, yielding a total volume of 10^3–10^4 m^3 of ejected gas and fragments during each Strombolian explosion. We demonstrate that the erupted ash volume is related to the total thermal energy, a relation which can then be efficiently used to estimate, in real-time, the volumetric eruptive flux. This has large implications for monitoring and risk assessment.

[64] The analysis of thermal images shows that the plume also expands radially but at a slower velocity of ∼80 m/s during the first 0.1 s. Eruption velocities are higher in the vertical rather than in the radial direction consistent with an explosive source mechanism controlled by the transport inside the conduit prior to its eruption.

[65] The time delay between the thermal onset and the acoustic signals (Δt_r) correlates with the inverse of the exit velocity (U) of the gas cloud supporting that infrasound is generated by explosive source dynamics within the conduit. The largest initial pressure peak is generated before the onset of emission with most of the acoustic energy being radiated before the plume reaches the vent exit.

[66] The peak amplitude of the acoustic pressure shows a power law ($p \sim U^2$) relationship with the exit velocity measured by thermal camera. Following the linear theory of sound [*Lighthill*, 1978], and in line with previous authors [e.g., *Vergniolle and Brandeis*, 1994; *Vergniolle and Caplan-Auerbach*, 2006; *Johnson*, 2003], we found that this power law relationship is in good agreement with the acoustic radiation from a monopole source with a radius of ∼2–3 m. This is consistent with our visual observation of the vent dimension during the experiment.

[67] The correlation between acoustic pressure generated inside the conduit and the eruptive cloud exit velocity measured at the vent by the thermal camera points to an explosive process that reaches the maximum velocity inside the conduit.

[68] Assuming that the vertical exit velocity (U) represents the maximum velocity reached by the explosive mixture inside the conduit, we use the reduced time delay (equation (6)) to locate the explosive source at depths (h_c) of <15 m and <35 m for the SW and NE crater, respectively.

[69] The linear theory of sound states that the excess pressure in the atmosphere is proportional to the acceleration of the volumetric change of the source. We infer that acoustic waves are then generated by the deformation of the magma free-surface which inflates during the fragmentation process. From the velocity history derived from the acoustic pressure (equation (10a)) we calculate that the magma surface inflates with accelerations in the order of 10^3–10^4 m/s^2. Duration of the infrasonic pulse indicates that this process lasts only for ∼0.1–0.3 s, but it triggers the much longer gas expansion outburst recorded by thermal camera (i.e., the sustained 4–5 s long gas thrust phase).

[70] Similar observations have been reported during laboratory experiments involving fragmentation of analogue porous materials generated by rapid decompression in a shock-tube [*Alidibirov and Panov*, 1998]. During these experiments, the duration of the fragmentation process (∼1–4 ms) was one order of magnitude shorter than the duration of the ejection stage (>15 ms). Fine particles were accelerated in the tube at $\sim 10^4$ m/s^2 by the fragmentation process to reach their maximum velocity (U_j) inside the conduit. In the shock-tube experiments, the maximum velocity of ejected fragments is a function ($\Delta p \sim U_j^2$) of the pressure differential Δp across the diaphragm, which is explained as the energy balance between the kinetic energy of the fragments and the potential energy of the compressed gas [*Alidibirov and Panov*, 1998]. The analogy between our field measurements and the fragmentation process in a shock-tube is intriguing and should be further investigated as potential alternative model to the bubble bursting process.

[71] **Acknowledgments.** We thank Giacomo Ulivieri, Diego Coppola, and Marco Laiolo for invaluable support in the field and scientific discussions on thermal images and acoustic waves. The manuscript has been improved by the reading of Andy Harris and by the critical comments of Matt Patrick, the Associate Editor and an anonymous reviewer.

References

Alidibirov, M., and V. Panov (1998), Magma fragmentation dynamics: Experiments with analogue porous low-strength material, *Bull. Volcanol.*, *59*, 481–489, doi:10.1007/s004450050205.

Allard, P., J. Carbonelle, N. Métrich, H. Loyer, and P. Zettwoog (1994), Sulphur output and magma degassing budget of Stromboli volcano, *Nature*, *368*, 326–330, doi:10.1038/368326a0.

Andronico, D., and M. Pistolesi (2010), The November 2009 paroxysmal explosions at Stromboli, *J. Volcanol. Geotherm. Res.*, *196*, 120–125, doi:10.1016/j.jvolgeores.2010.06.005.

Barberi, F., L. Civetta, M. Rosi, and P. Scandone (2009), Chronology of the 2007 eruption of Stromboli and the activity of the Scientific Synthesis Group, *J. Volcanol. Geotherm. Res.*, *182*, 123–130, doi:10.1016/j.jvolgeores.2008.09.019.

Blackburn, E. A., L. Wilson, and R. S. J. Sparks (1976), Mechanisms and dynamics of strombolian activity, *J. Geol. Soc.*, *132*, 429–440, doi:10.1144/gsjgs.132.4.0429.

Caplan-Auerbach, J., A. Bellesiles, and J. K. Fernandes (2010), Estimates of eruption velocity and plume height from infrasonic recordings of the 2006 eruption of Augustine Volcano, Alaska, *J. Volcanol. Geotherm. Res.*, *189*, 12–18, doi:10.1016/j.jvolgeores.2009.10.002.

Chouet, B., N. Hamisevicz, and T. R. McGetchin (1974), Photoballistics of volcanic jet activity at Stromboli, Italy, *J. Geophys. Res.*, *79*, 4961–4976, doi:10.1029/JB079i032p04961.

Fagents, S. A., and L. Wilson (1993), Explosive volcanic eruptions, VII. The ranges of pyroclastic ejected in transient volcanic explosions, *Geophys. J. Int.*, *113*, 359–370, doi:10.1111/j.1365-246X.1993.tb00892.x.

Garcés, M. A. (2000), Theory of acoustic propagation in a multi-phase stratified liquid flowing within an elastic-walled conduit of varying cross-sectional area, *J. Volcanol. Geotherm. Res.*, *101*, 1–17, doi:10.1016/S0377-0273(00)00155-4.

Harris, A. J. L., and M. Ripepe (2007), Synergy of multiple geophysical approaches to unravel explosive eruption conduit and source dynamics: A case study for Stromboli, *Chem. Erde*, *67*, 1–35, doi:10.1016/j.chemer.2007.01.003.

Harris, A. J. L., and D. S. Stevenson (1997), Thermal observations of degassing open conduits and fumaroles at Stromboli and Vulcano using remotely sensed data, *J. Volcanol. Geotherm. Res.*, *76*, 175–198, doi:10.1016/S0377-0273(96)00097-2.

Harris, A. J. L., et al. (2005), DUCKS: Low cost thermal monitoring units for near-vent deployment, *J. Volcanol. Geotherm. Res.*, *143*, 335–360, doi:10.1016/j.jvolgeores.2004.12.007.

Harris, A. J. L., M. Ripepe, and E. E. Hughes (2012), Detailed analysis of particle launch velocities, size distributions and gas densities during normal explosions at Stromboli, *J. Volcanol. Geotherm. Res.*, *231–232*, 109–131, doi:10.1016/j.jvolgeores.2012.02.012.

Hort, M., R. Seyfried, and M. Vöge (2003), Radar Doppler velocimetry of volcanic eruptions: Theoretical considerations and quantitative documentation of changes in eruptive behaviour at Stromboli volcano, Italy, *Geophys. J. Int.*, *154*, 515–532, doi:10.1046/j.1365-246X.2003.01982.x.

Johnson, J. B. (2003), Generation and propagation of infrasonic airwaves from volcanic explosions, *J. Volcanol. Geotherm. Res.*, *121*, 1–14, doi:10.1016/S0377-0273(02)00408-0.

Johnson, J. B. (2007), On the relation between infrasound, seismicity, and small pyroclastic explosions at Karymsky Volcano, *J. Geophys. Res.*, *112*, B08203, doi:10.1029/2006JB004654.

Johnson, J. B., R. Aster, K. R. Jones, P. Kyle, and B. McIntosh (2008), Acoustic source characterization of impulsive Strombolian eruptions from the Mount Erebus lava lake, *J. Volcanol. Geotherm. Res.*, *177*(3), 673–686, doi:10.1016/j.jvolgeores.2008.06.028.

Kobayashi, T., Y. Ida, and T. Ohminato (2005), Small inflation sources producing seismic and infrasonic pulses during the 2000 eruptions of Miyake-jima, Japan, *Earth Planet. Sci. Lett.*, *240*, 291–301, doi:10.1016/j.epsl.2005.09.015.

Lighthill, M. J. (1978), *Waves in Fluids*, 504 pp., Cambridge Univ. Press, New York.

Marchetti, E., M. Ripepe, A. J. L. Harris, and D. Delle Donne (2009), Tracing the differences between Vulcanian and Strombolian explosions using infrasonic and thermal radiation energy, *Earth Planet. Sci. Lett.*, *279*, 273–281, doi:10.1016/j.epsl.2009.01.004.

Matoza, R. S., D. Fee, and M. Garces (2010), Infrasonic tremor wavefield of the Pu'u O'o crater complex and lava tube system, Hawaii, in April 2007, *J. Geophys. Res.*, *115*, B12312, doi:10.1029/2009JB007192.

Mori, T., and M. Burton (2009), Quantification of the gas mass emitted during single explosions on Stromboli with the SO_2 imaging camera, *J. Volcanol. Geotherm. Res.*, *188*, 395–400, doi:10.1016/j.jvolgeores.2009.10.005.

Patrick, M. R. (2005), Strombolian eruption dynamics from thermal (FLIR) video imagery, PhD thesis, Geol. and Geophys., Univ. of Hawaii, Honolulu.

Patrick, M. R. (2007), Dynamics of Strombolian ash plumes from thermal video: Motion, morphology, and air entrainment, *J. Geophys. Res.*, *112*, B06202, doi:10.1029/2006JB004387.

Petersen, T., and S. R. McNutt (2007), Seismo-acoustic signals associated with degassing explosions recorded at Shishaldin Volcano, Alaska, 2003–2004, *Bull. Volcanol.*, *69*, 527–536, doi:10.1007/s00445-006-0088-z.

Pistolesi, M., D. Delle Donne, L. Pioli, M. Rosi, and M. Ripepe (2011), The 15 March 2007 explosive crisis at Stromboli Volcano, Italy: Assessing physical parameters through a multidisciplinary approach, *J. Geophys. Res.*, *116*, B12206, doi:10.1029/2011JB008527.

Ripepe, M., M. Rossi, and G. Saccorotti (1993), Image processing of explosive activity at Stromboli, *J. Volcanol. Geotherm. Res.*, *54*, 335–351, doi:10.1016/0377-0273(93)90071-X.

Ripepe, M., S. Ciliberto, and M. Della Schiava (2001), Time constraints for modeling source dynamics of volcanic explosions at Stromboli, *J. Geophys. Res.*, *106*(B5), 8713–8727, doi:10.1029/2000JB900374.

Ripepe, M., D. Delle Donne, A. Harris, E. Marchetti, and G. Ulivieri (2008), Dynamics of Strombolian activity, in *The Stromboli Volcano: An Integrated Study of the 2002–2003 Eruption, Geophys. Monogr. Ser*, vol. 182, edited by S. Calvari et al., pp. 39–48, AGU, Washington, D. C.

Ruiz, M., J. M. Lees, and J. B. Johnson (2006), Source constraints of Tungurahua volcano explosion events, *Bull. Volcanol.*, *68*, 480–490, doi:10.1007/s00445-005-0023-8.

Scharff, L., M. Hort, A. J. L. Harris, M. Ripepe, J. M. Lees, and R. Seyfried (2008), Eruption dynamics of the SW crater of Stromboli volcano, Italy: An interdisciplinary approach, *J. Volcanol. Geotherm. Res.*, *176*, 565–570, doi:10.1016/j.jvolgeores.2008.05.008.

Seyfried, R., and M. Hort (1999), Continuous monitoring of volcanic eruption dynamics: A review of various techniques and new results from a frequency: Modulated radar Doppler system, *Bull. Volcanol.*, *60*, 627–639, doi:10.1007/s004450050256.

Steinberg, G. S., and J. I. Babenko (1978), Experimental velocity and density determination of volcanic gases during eruption, *J. Volcanol. Geotherm. Res.*, *3*, 89–98, doi:10.1016/0377-0273(78)90005-7.

Taddeucci, J., P. Scarlato, A. Capponi, E. Del Bello, C. Cimarelli, D. M. Palladino, and U. Kueppers (2012), High-speed imaging of Strombolian explosions: The ejection velocity of pyroclasts, *Geophys. Res. Lett.*, *39*, L02301, doi:10.1029/2011GL050404.

Vergniolle, S., and G. Brandeis (1994), Origin of the sound generated by strombolian explosions, *Geophys. Res. Lett.*, *21*, 1959–1962, doi:10.1029/94GL01286.

Vergniolle, S., and J. Caplan-Auerbach (2006), Basaltic thermals and subplinian plumes: Constraints from acoustic measurements at Shishaldin volcano, Alaska, *Bull. Volcanol.*, *68*, 611–630, doi:10.1007/s00445-005-0035-4.

Weill, A., G. Brandeis, S. Vergniolle, F. Baudin, J. Bilbille, J. Fevre, B. Piron, and X. Hill (1992), Acoustic sounder measurements of the vertical velocity of volcanic jets at Stromboli volcano, *Geophys. Res. Lett.*, *19*, 2357–2360, doi:10.1029/92GL02502.

Wilson, L. (1980), Relationships between pressure, volatile content and ejecta velocity in three types of volcanic explosion, *J. Volcanol. Geotherm. Res.*, *8*, 297–313, doi:10.1016/0377-0273(80)90110-9.

Woulff, G., and T. R. McGetchin (1976), Acoustic noise from volcanoes: Theory and experiments, *Geophys. J. R. Astron. Soc.*, *45*, 601–616, doi:10.1111/j.1365-246X.1976.tb06913.x.